PHYSICAL REVIEW LETTERS **132,** 226704 (2024)

Efficient Magnon Injection and Detection via the Orbital Rashba-Edelstein Effect

J. A. Mendoza-Rodarte,[1,2] M. Cosset-Chéneau,[1,*] B. J. van Wees,[1] and M. H. D. Guimarães[1]
[1]*Zernike Institute for Advanced Materials, University of Groningen, 9747 AG Groningen, The Netherlands*
[2]*Centro de Nanociencias y Nanotecnología-Universidad Nacional Autónoma de México, Ensenada, 22800-Baja California, México*

(Received 14 December 2023; revised 13 April 2024; accepted 25 April 2024; published 31 May 2024)

Orbital currents and accumulation provide a new avenue to boost spintronic effects in nanodevices. Here, we use interconversion effects between charge current and orbital angular momentum to demonstrate a dramatic increase in the magnon spin injection and detection efficiencies in nanodevices consisting of a magnetic insulator contacted by $\mathrm{Pt/CuO_x}$ electrodes. Moreover, we note distinct variations in efficiency for magnon spin injection and detection, indicating a disparity in the direct and inverse orbital Rashba-Edelstein effect efficiencies.

DOI: 10.1103/PhysRevLett.132.226704

Magnon transport in nonlocal devices [1,2] is an efficient way of probing the collective excitation of the magnetic order in a variety of materials such as ferrimagnets [3–6], antiferromagnetic oxides [7–9], and Van der Waals materials [10]. It permits one to access the near equilibrium magnon transport properties in the diffusive regime [11], thus uncovering a new type of nonlinear phenomenon such as the magnon diode effect [12,13], while also providing a way to study thermally driven magnon transport effects [14–16] and nonreciprocal magnon transport [17–19]. Finally, it allows one to electrically control a magnon population [20,21] and opens the possibility to realize magnon transistors [22]. This, however, relies on the possibility of efficiently injecting and detecting magnons with a static electrical current using interfacial spin transfer effects [23]. So far, nonlocal magnon transport devices have relied on the direct and inverse spin Hall effect (SHE) [24] in Pt, which has provided only small nonlocal signals, thus limiting the application range of this method. This is particularly problematic for materials with short magnon relaxation lengths, such as Van der Waals magnets, since the signals are often too small to explore new functionalities in magnonic devices.

The recent demonstrations [25–33] that spin-charge interconversion effects can be strongly increased by exploiting the orbital angular momentum [34] may, however, lift this limitation. It has been reported that an orbital current, which is a flux of orbital angular momentum, can be generated with a large efficiency by a charge current through orbital Hall effects in light metals [35–37], or by the direct orbital Rashba-Edelstein effects (OREE) at metal oxide interfaces [38–41]. This orbital current is then converted into a spin current by the spin-orbit coupling of either a heavy metal or within the ferromagnet, and is then able to apply a torque on the ferromagnet's magnetization [27,39,42–44]. The reports that an orbital current can also be efficiently converted into a charge current by the inverse orbital Hall effect [45–47] or the inverse OREE at a $\mathrm{Pt/CuO_x}$ interface [48–50] open the possibility of achieving large signals in nonlocal magnon transport devices and hence greatly expanding their range of application. However, nonlocal magnon transport devices exploiting interfacial orbital effects have not yet been explored. This also permits one to probe the efficiencies of the direct and inverse OREE in the same device. These efficiencies are defined as the ratio of the generated spin current over the applied charge current for the direct OREE and as the ratio of the generated charge current over the applied spin current for the inverse OREE. The possibility of these two ratios being different for interconversion effects taking place at the interface has been heavily debated [51] in the context of the spin-to-charge interconversion. In addition, recent orbital pumping experiments [45,47] have shown that different mechanisms may be at play in the orbital-to-charge and charge-to-orbital interconversion effects, hence leading to differences in the efficiency between these interconversion effects.

Here, we demonstrate a dramatic increase in the output signal of yttrium iron garnet ($\mathrm{Y_3Fe_5O_{12}}$—YIG) based nonlocal magnon transport nanodevices by exploiting the OREE at the $\mathrm{Pt/CuO_x}$ interface [39,49,52]. By comparing the different magnon generation and detection processes in these devices [Fig. 1(a)], we obtain indications that the interconversion by the OREE of a charge current into an orbital current and of an orbital current into a charge current do not have the same efficiencies.

The nonlocal magnon transport devices, consisting of two $\mathrm{Pt}(t_{\mathrm{Pt}})/\mathrm{CuO_x}(3\ \mathrm{nm})$ magnon injecting and detecting electrodes, were fabricated on a 150 nm-thick YIG single crystal (Matesy GmbH) grown by liquid phase epitaxy on a $\mathrm{Gd_3Ga_5O_{12}}$ (GGG) substrate with (111) orientation. The edge-to-edge distance between the 400 nm-wide 80 μm-long electrodes is fixed for all devices at 2 μm. The devices were fabricated by conventional lithography processes,

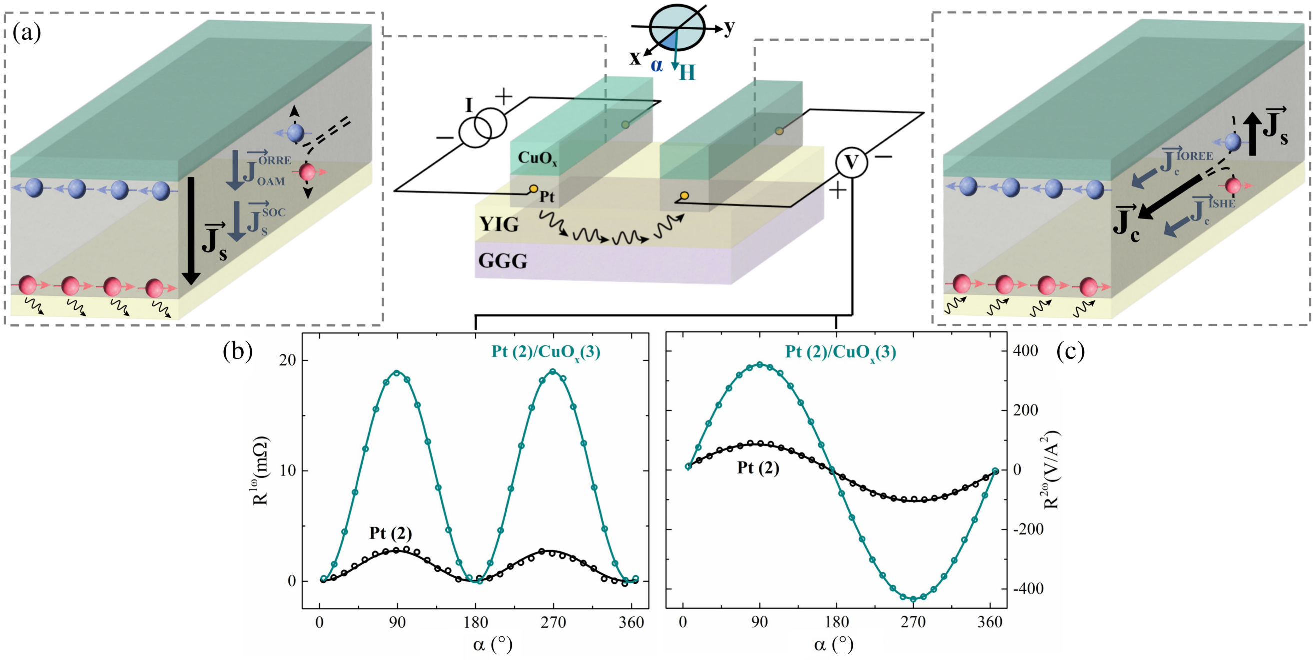

FIG. 1. (a) Left: contribution of the direct OREE to the charge to spin interconversion process. The OREE generates an orbital accumulation at the Pt/CuO$_x$ interface, which diffuses as an orbital current ($\boldsymbol{J}_{\mathrm{OAM}}^{\mathrm{OREE}}$) into the Pt layer. It is then converted into a spin current ($\boldsymbol{J}_s^{\mathrm{SOC}}$) and adds up to the one produced by the SHE to form a total spin current $\boldsymbol{J}_s$ which generates a magnon accumulation in YIG. Center: schematic of the nonlocal magnon transport device with its electrical interconnects and the external magnetic field angle α. Right: contribution of the inverse OREE to the spin-to-charge interconversion process. The spin current $\boldsymbol{J}_s$ created by the magnon accumulation is converted into a charge current $\boldsymbol{J}_c^{\mathrm{SHE}}$ by the SHE in Pt and into an orbital accumulation at the Pt/CuO$_x$ interface. The inverse OREE generates a charge current $\boldsymbol{J}_c^{\mathrm{OREE}}$, with both effects resulting in a total charge current $\boldsymbol{J}_c$. First (b) and second (c) harmonic resistance response as a function of α. The green and black data points correspond to devices with Pt/CuO$_x$ and Pt electrodes respectively, both with $t_{Pt} = 2$ nm. A baseline has been removed, so that the nonlocal signals are zero at $\alpha = 0$ and 180°.

followed by the dc sputtering in Ar$^+$ plasma of Pt and Cu and by a subsequent liftoff. All the electrodes were patterned during the same lithography level to ensure the consistency of the YIG/Pt interface quality, and the depositions of the different stacks were performed separately for the different devices. The YIG surface was cleaned using an Ar$^+$ etching step prior to the deposition. The devices were left in ambient conditions for two days to achieve a natural oxidation of the Cu layer. The measurements were performed by rotating an external magnetic field (70 mT) in the plane of the device. We use a conventional lock-in detection technique with a bias current (I_{bias}) of 70 μA applied in the injecting electrode at a frequency of 5.1 Hz to measure the first ($V^{1\omega}$) and second ($V^{2\omega}$) nonlocal voltage responses at the detecting electrodes—see Fig. 1(a) for the electrical interconnects. All measurements were performed at room temperature.

Figures 1(b) and 1(c) show the magnetic field angle (α) dependence of the first ($R^{1\omega} = V^{1\omega}/I_{\mathrm{bias}}$) and second ($R^{2\omega} = V^{2\omega}/I_{\mathrm{bias}}^2$) harmonic nonlocal signals, respectively, measured on devices using Pt(2) and Pt(2)/CuO$_x$(3) electrodes. The signals can be fitted using $R^{1\omega} = R_{\mathrm{nl}}^{1\omega}\sin^2(\alpha)$ and $R^{2\omega} = R_{\mathrm{nl}}^{2\omega}\sin(\alpha)$, which give the amplitude $R_{\mathrm{nl}}^{1\omega}$ and $R_{\mathrm{nl}}^{2\omega}$ of the first and second harmonic nonlocal signal [1]. Here, we define $R_{\mathrm{nl,Pt}}^{1(2)\omega}$ and $R_{\mathrm{nl,CuO_x}}^{1(2)\omega}$ as the amplitudes of the first (second) harmonic nonlocal signal measured in devices with Pt only and Pt/CuO$_x$ electrodes, respectively. For $t_{Pt} = 2$ nm, the nonlocal signal amplitudes strongly depend on the presence of the CuO$_x$ layer, with the first harmonic signal going from 2.71 mΩ for Pt-only electrodes to 19.14 mΩ for Pt/CuO$_x$ electrodes, i.e., a factor of 7 increase in the signal. Similarly, the second harmonic nonlocal resistance goes from 95.4 to 391.3 VA^{-2} , a factor of 4 increase. When increasing the thickness of Pt, a strong decrease of both $R_{\mathrm{nl,CuO_x}}^{1\omega}$ and $R_{\mathrm{nl,CuO_x}}^{2\omega}$ occurs [Figs. 2(a) and 2(b)], and the difference between devices with Pt and Pt/CuO$_x$ electrodes becomes less important. This is consistent with the picture discussed in Fig. 1(a), where, in order for the OREE to play a role in the magnon injection and detection processes, the thickness of the Pt layer should be much smaller than the spin relaxation length.

To quantify the charge-to-spin interconversion efficiencies as a function of the thickness of the Pt layer, the electrical resistance of the electrodes needs to be taken into account, since this influences the measured voltage. The nonlocal signals depend on the detecting electrode two point resistance (R_{2p}) as $R^{1\omega} = I^{1\omega}R_{\mathrm{2p}}/I_{\mathrm{bias}}$, and

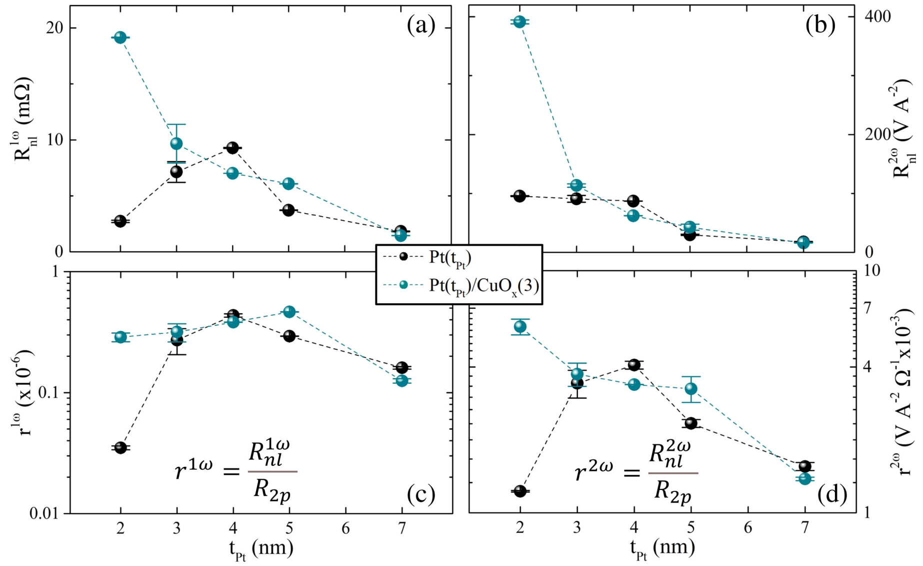

FIG. 2. First (a) and second (b) harmonic nonlocal signal amplitudes as a function of the Pt layer thickness (t_{Pt}). (c) First and (d) second harmonic nonlocal spin signal amplitudes normalized by the two point resistance of the detecting electrode as a function of t_{Pt}. The green data points correspond to devices with $\mathrm{Pt/CuO_x}$ electrodes, while the black data points are for Pt-only electrodes.

$R^{2\omega} = I^{2\omega} R_{2\mathrm{p}} / I^2_{\mathrm{bias}}$ with $I^{1(2)\omega}$ being the first (second) harmonic charge current generated by the spin-to-charge interconversion processes at the detecting electrode. In Figs. 2(c) and 2(d) we plot the first and second harmonic nonlocal signals' amplitudes normalized by the two point resistance of the detecting electrode, $r^{n\omega}_{\sigma} = R^{n\omega}_{\mathrm{nl},\sigma}/R_{2\mathrm{p}}$ with $n = 1, 2$ and $\sigma = \mathrm{Pt}$ or $\mathrm{Pt/CuO_x}$. The normalized first and second harmonic nonlocal signals for Pt-only devices, $r^{1\omega}_{\mathrm{Pt}}$ and $r^{2\omega}_{\mathrm{Pt}}$, display strong drops of nearly an order of magnitude when the Pt thickness is reduced from 3 to 2 nm. This behavior contrasts with the one observed in devices using $\mathrm{Pt/CuO_x}$ electrodes, where there is only a slight decrease in $r^{1\omega}_{\mathrm{CuO_x}}$ while $r^{2\omega}_{\mathrm{CuO_x}}$ increases when t_{Pt} goes from 3 to 2 nm. The difference between the normalized nonlocal signals obtained with and without $\mathrm{CuO_x}$ layers vanishes when the Pt thickness increases beyond 3 nm. These results match previous reports of the OREE at $\mathrm{Pt/CuO_x}$ interfaces [39,49], which attributed the thickness dependence of the signals to interconversion and relaxation of spin and orbital currents over the spin and orbital diffusion length. This directly demonstrates that the presence of a $\mathrm{Pt/CuO_x}$ interface leads to an increase of the spin-charge interconversion processes' efficiency in the magnon injecting and detecting electrodes with respect to Pt-only electrodes.

The spin-charge interconversion processes in the $\mathrm{Pt/CuO_x}$ electrodes possess contributions from the SHE in Pt, and from the charge-orbital interconversion by the OREE at the $\mathrm{Pt/CuO_x}$ interface [39,49]. We also point out that even if the 3 nm Cu layer does not fully oxidize in ambient conditions [52], a strong OREE at the $\mathrm{Cu/CuO_x}$ interface is also expected [29]. In the injecting electrode, the direct OREE contributes to the charge to spin interconversion by inducing an orbital accumulation at the $\mathrm{Pt/CuO_x}$ interface, which then creates an orbital current converted into a spin current by the spin-orbit coupling [39] when flowing into the Pt layer [Fig. 1(a), left panel]. This spin current then crosses the Pt/YIG interface inducing a magnon accumulation under the injecting electrode. After propagation, the magnon accumulation under the detecting electrode creates a spin current that flows into Pt and is partially converted into an orbital current via the high spin-orbit coupling of Pt. The orbital current then creates an orbital accumulation at the $\mathrm{Pt/CuO_x}$ interface and subsequently a charge current by the inverse OREE [Fig. 1(a), right panel]. In addition, the SHE in Pt contributes to the spin-to-charge interconversion processes. While the direct and inverse interconversion efficiencies by the SHE were demonstrated to be the same [53], our observations point to the fact that this is not the case for the OREE.

To better quantify the contribution of the direct and inverse OREE to the spin-to-charge interconversion in the $\mathrm{Pt/CuO_x}$ electrodes and explore their (different) efficiencies, we make use of the nonlocal signals created by electrically and thermally generated magnons [54]. While the electrically injected magnons depend on the spin-to-charge interconversion efficiency of the injector electrode, thermally injected magnons only depend on the Joule heating generated at the injection point. Assuming that the detection process is the same (see Supplemental Material [55] for details), the signals from the electrically injected magnons depend on both the injector and detector (i.e., direct and inverse charge-to-spin conversion) efficiencies, while for thermally generated magnons the signals are only dependent on the detection (inverse charge-to-spin conversion) efficiency. These two magnon populations are detected as the first and second harmonic responses [1] with the angular dependences shown in Figs. 1(b) and 1(c), respectively.

We highlight the asymmetry in the injection and detection processes by using a simple magnon diffusive picture that can be described as follows. The electrical current flowing in the injecting electrode generates a spin current $j_{\mathrm{inj}}^{\mathrm{elec}} = \kappa^D I_{\mathrm{bias}}$ that flows across the YIG-Pt interface, with κ^D the efficiency of the charge-to-spin interconversion, containing both SHE and OREE contributions. This creates an electrically generated magnon accumulation which diffuses toward the detecting electrode, producing a spin current $j_{\mathrm{det}}^{\mathrm{elec}} = T_{\mathrm{YIG}} j_{\mathrm{inj}}^{\mathrm{elec}}$ at its interface with YIG [11]. For simplicity, here T_{YIG} contains all the magnon spin transport parameters of YIG and across the YIG/Pt interfaces, such as the magnon conductivity and the spin mixing conductance. The spin current in the detecting electrode ($j_{\mathrm{det}}^{\mathrm{elec}}$), generated by electrical magnon spin injection, is detected as the charge current $I^{1\omega} = \kappa^I j_{\mathrm{det}}^{\mathrm{elec}}$, with κ^I being the efficiency of the spin-to-charge interconversion. The thermal gradient caused by the bias current at the injector electrode creates a flow of thermally generated magnons in YIG and a spin current $j_{\mathrm{det}}^{\mathrm{therm}} = T_{\mathrm{YIG}}^{\mathrm{therm}} I_{\mathrm{bias}}^2$ at the YIG/Pt interface of the detection electrode [14,58]. Here, $T_{\mathrm{YIG}}^{\mathrm{therm}}$ is a combination of the thermal transport parameters in YIG and can be used for a linear response of the system to a thermal gradient [59]; see Ref. [55] for details. The thermally generated spin current is converted into a charge current $I^{2\omega} = \kappa^I j_{\mathrm{det}}^{\mathrm{therm}}$ at the detecting electrode. The first and second harmonic normalized nonlocal responses, $r^{1\omega} = I^{1\omega}/I_{\mathrm{bias}}$ and $r^{2\omega} = I^{2\omega}/I_{\mathrm{bias}}^2$, respectively, are therefore

$$r^{1\omega} = \kappa^D T_{\mathrm{YIG}} \kappa^I, \tag{1}$$

and

$$r^{2\omega} = T_{\mathrm{YIG}}^{\mathrm{therm}} \kappa^I, \tag{2}$$

with κ^D and κ^I the only parameters that depend on the spin-charge interconversion processes in the injecting and detecting electrodes. In the following, we note $\kappa_{\mathrm{Pt}}^{D(I)}$ as the direct (inverse) interconversion efficiencies for the Pt-only electrodes and $\kappa_{\mathrm{CuO_x}}^{D(I)}$ as the direct (inverse) interconversion efficiencies for the Pt/CuO$_x$ electrodes. Since the direct and inverse spin-to-charge interconversion effects are expected to have the same efficiencies for the SHE, $\kappa_{\mathrm{Pt}}^D = \kappa_{\mathrm{Pt}}^I$. Finally, the magnon transport properties of YIG, T_{YIG} and $T_{\mathrm{YIG}}^{\mathrm{therm}}$, are assumed to be independent of the presence of a CuO$_x$ layer on the electrodes. In addition, we assume that the presence of a CuO$_x$ layer on top of Pt does not open an additional spin relaxation channel and that it does not significantly alter the thermal gradient with respect to the one present in devices using Pt-only electrodes.

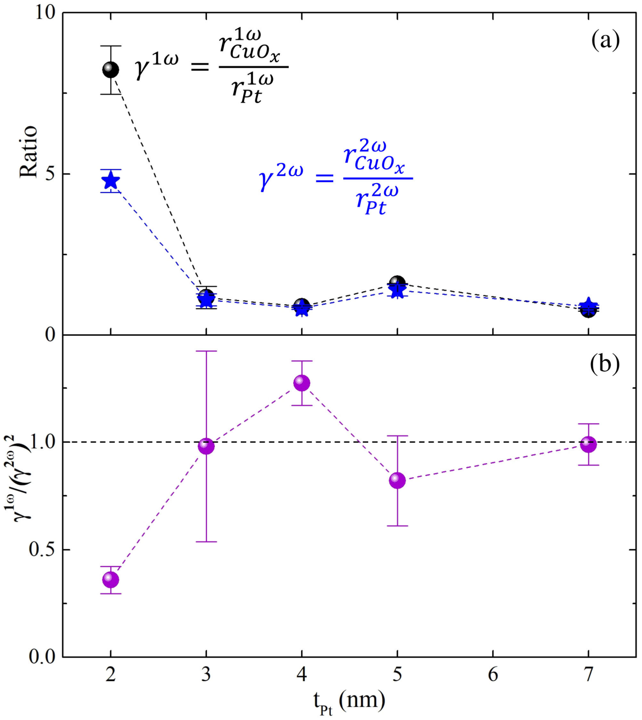

FIG. 3. (a) $\gamma^{1\omega}$ (black circles) and $\gamma^{2\omega}$ (blue stars) and (b) $\gamma^{1\omega}/(\gamma^{2\omega})^2$ as function of t_{Pt}.

The spin-to-charge interconversion efficiencies in the Pt and Pt/CuO$_x$ electrodes for injection and detection can be directly compared by plotting $\gamma^{1\omega} = r_{\mathrm{CuO_x}}^{1\omega}/r_{\mathrm{Pt}}^{1\omega}$ and $\gamma^{2\omega} = r_{\mathrm{CuO_x}}^{2\omega}/r_{\mathrm{Pt}}^{2\omega}$ [Fig. 3(a)]. The charge current generated at the detecting electrode by the electrically generated magnons ($\gamma^{1\omega}$) shows an increase of a factor of 8 for $t_{\mathrm{Pt}} = 2$ nm in the presence of a CuO$_x$ capping layer with respect to uncapped electrodes. In contrast, the charge current at the detector electrode obtained by thermally generated magnons ($\gamma^{2\omega}$) shows an increase of a factor of 5. No significant increase of the generated first and second harmonic charge current is observed for $t_{\mathrm{Pt}} = 3$ and 5 nm, and $\gamma^{1\omega} \approx \gamma^{2\omega} \sim 1$. This indicates that for a Pt thickness larger than its spin relaxation length (∼2 nm), the presence of a CuO$_x$ capping layer has no effect on our signals, indicating that the OREE does not contribute to the spin-to-charge interconversion. This is in agreement with previous reports on other types of measurements [39,49,52]. Nonetheless, none of these reports have been able to detect and separate the direct and inverse OREE in the same device.

The electrical magnon spin injection depends on both the direct and inverse charge-to-spin interconversion efficiencies, while the signals generated by thermally injected magnons depend only on the inverse interconversion efficiency. The efficiencies of the direct and inverse charge-to-spin interconversion processes can be quantified by the ratio

$$\frac{\gamma^{1\omega}}{(\gamma^{2\omega})^2} = \frac{\kappa^D_{\mathrm{CuO_x}}}{\kappa^I_{\mathrm{CuO_x}}}.$$

If we assume a similar efficiency for the direct ($\kappa^D_{\mathrm{CuO_x}}$) and inverse ($\kappa^I_{\mathrm{CuO_x}}$) OREE-assisted spin-charge interconversion effects, this implies that $\gamma^{1\omega} = (\gamma^{2\omega})^2$ or $\kappa^D_{\mathrm{CuO_x}} = \kappa^I_{\mathrm{CuO_x}}$. This is in stark contrast with the observations for devices with $t_{\mathrm{Pt}} = 2$ nm [Fig. 3(b)], where $\gamma^{1\omega}/(\gamma^{2\omega})^2 = 0.4$, clearly indicating an asymmetry in the injection and detection processes in these devices.

We thus conclude that the efficiency of the orbital-to-charge interconversion by the OREE appears to be larger than the efficiency of the charge-to-orbital interconversion by this same effect, i.e., $\kappa^I_{\mathrm{CuO_x}} = 0.4\kappa^D_{\mathrm{CuO_x}}$. We stress that these conclusions rely on a few assumptions regarding the possibility of comparing the first and second harmonic nonlocal signals, owing to the difference in magnon generation processes. This is discussed in detail in Ref. [55]. This situation is reminiscent of the previously observed different efficiencies of the spin-charge interconversions by the Rashba-Edelstein effect at a metal oxide interface [51], which was attributed to the different scattering times within the interfacial states and in the metallic bulk. Our results indicate that a similar mechanism might be at play in the OREE at metal oxide interfaces. In addition, reports of alternative spin-to-charge interconversion mechanisms could explain our results. In particular, it was demonstrated that the presence of an oxidation gradient in Cu could result in different direct and inverse spin-to-charge interconversion efficiencies [60]. Finally, taking into account the different length scales observed in charge-to-orbital [35] and orbital-to-charge [45] interconversion experiments could shed light on these results.

We envision that the use of the OREE to increase nonlocal magnon signals by nearly 1 order of magnitude, as we show here, can be used to expand the range of materials for magnon transport. This includes, for example, materials with short magnon relaxation lengths for which nonlocal magnon signals tend to be very small, but might still show interesting magnonic effects. Furthermore, the possibility of generating very large magnon accumulations should give easier access to nonlinear magnonic phenomena such as magnon condensates [61] and spin diodes [12]. The use of the orbital degree of freedom can also be used to study the transport of collective orbital excitations in insulating materials [62] using nonlocal devices. Finally, the use of these devices to show the difference between the direct and inverse interconversion efficiencies in orbital-assisted interconversion processes will help achieve a better understanding of charge-orbital interconversion effects.

We acknowledge the technical support of J. Holstein, H. de Vries, F. H. van der Velde, H. Adema, and A. Joshua. This work was supported by the Dutch Research Council (NWO—OCENW.XL21.XL21.058), the Zernike Institute for Advanced Materials, the research program "Materials for the Quantum Age" (QuMat, registration No. 024.005.006), which is part of the Gravitation program financed by the Dutch Ministry of Education, Culture and Science (OCW), and the European Union (ERC, 2D-OPTOSPIN, 101076932, and 2DMAGSPIN, 101053054). Views and opinions expressed are, however, those of the author(s) only and do not necessarily reflect those of the European Union or the European Research Council. Neither the European Union nor the granting authority can be held responsible for them. J. A. M. R. acknowledges the financial support of Consejo Nacional de Humanidades, Ciencias y Tecnologías (CONAHCYT) for a graduate research fellowship (No. CVU 655591). The device fabrication and characterization were performed using Zernike NanoLabNL facilities.

---

[*]Corresponding author: m.n.c.g.cosset-cheneau@rug.nl

[1] L. J. Cornelissen, J. Liu, R. A. Duine, J. Ben Youssef, and B. J. van Wees, Long-distance transport of magnon spin information in a magnetic insulator at room temperature, Nat. Phys. **11**, 1022 (2015).

[2] M. Althammer, All-electrical magnon transport experiments in magnetically ordered insulators, Phys. Status Solidi RRL **15**, 2100130 (2021).

[3] L. J. Cornelissen, J. Shan, and B. J. van Wees, Temperature dependence of the magnon spin diffusion length and magnon spin conductivity in the magnetic insulator yttrium iron garnet, Phys. Rev. B **94**, 180402(R) (2016).

[4] X. Y. Wei, O. A. Santos, C. H. S. Lusero, G. E. W. Bauer, J. Ben Youssef, and B. J. van Wees, Giant magnon spin conductivity in ultrathin yttrium iron garnet films, Nat. Mater. **21**, 1352 (2022).

[5] M. X. Aguilar-Pujol, S. Catalano, C. González-Orellana, W. Skowroński, J. M. Gomez-Perez, M. Ilyn, C. Rogero, M. Gobbi, L. E. Hueso, and F. Casanova, Magnon currents excited by the spin Seebeck effect in ferromagnetic EuS thin films, Phys. Rev. B **108**, 224420 (2023).

[6] J. Gao, C. H. Lambert, R. Schlitz, M. Fiebig, P. Gambardella, and S. Vélez, Magnon transport and thermoelectric effects in ultrathin $\mathrm{Tm_3Fe_5O_{12}}$ /Pt nonlocal devices, Phys. Rev. Res. **4**, 043214 (2022).

[7] R. Li, L. J. Riddiford, Y. Chai, M. Dai, H. Zhong, B. Li, P. Li, D. Yi, Y. Zhang, D. A. Broadway, A. E. E. Dubois, P. Maletinsky, J. Hu, Y. Suzuki, D. C. Ralph, and T. Nan, A puzzling insensitivity of magnon spin diffusion to the presence of 180-degree domain walls, Nat. Commun. **14**, 2393 (2023).

[8] R. Lebrun, A. Ross, S. A. Bender, A. Qaiumzadeh, L. Baldrati, J. Cramer, A. Brataas, R. A. Duine, and M. Kläui, Tunable long-distance spin transport in a crystalline antiferromagnetic iron oxide, Nature (London) **561**, 222 (2018).

[9] J. Shan, P. Bougiatioti, L. Liang, G. Reiss, T. Kuschel, and B. J. van Wees, Nonlocal magnon spin transport in $\mathrm{NiFe_2O_4}$ thin films, Appl. Phys. Lett. **110**, 132406 (2017).

[10] D. K. de Wal, A. Iwens, T. Liu, P. Tang, G. E. W. Bauer, and B. J. van Wees, Long-distance magnon transport in the van der Waals antiferromagnet $CrPS_4$, Phys. Rev. B **107**, L180403 (2023).

[11] L. J. Cornelissen, K. J. H. Peters, G. E. W. Bauer, R. A. Duine, and B. J. van Wees, Magnon spin transport driven by the magnon chemical potential in a magnetic insulator, Phys. Rev. B **94**, 014412 (2016).

[12] R. Kohno, K. An, E. Clot, V. V. Naletov, N. Thiery, L. Vila, R. Schlitz, N. Beaulieu, J. Ben Youssef, A. Anane, V. Cros, H. Merbouche, T. Hauet, V. E. Demidov, S. O. Demokritov, G. de Loubens, and O. Klein, Nonlocal magnon transconductance in extended magnetic insulating films. I. Spin diode effect, Phys. Rev. B **108**, 144410 (2023).

[13] R. Kohno, K. An, E. Clot, V. V. Naletov, N. Thiery, L. Vila, R. Schlitz, N. Beaulieu, J. Ben Youssef, A. Anane, V. Cros, H. Merbouche, T. Hauet, V. E. Demidov, S. O. Demokritov, G. de Loubens, and O. Klein, Nonlocal magnon transconductance in extended magnetic insulating films. II. Two-fluid behavior, Phys. Rev. B **108**, 144411 (2023).

[14] J. Shan, L. J. Cornelissen, J. Liu, J. Ben Youssef, L. Liang, and B. J. van Wees, Criteria for accurate determination of the magnon relaxation length from the nonlocal spin Seebeck effect, Phys. Rev. B **96**, 184427 (2017).

[15] F. Feringa, J. M. Vink, and B. J. van Wees, Spin Nernst magnetoresistance for magnetization study of $FePS_3$, Phys. Rev. B **107**, 094428 (2023).

[16] G. R. Hoogeboom and B. J. van Wees, Nonlocal spin Seebeck effect in the bulk easy-plane antiferromagnet NiO, Phys. Rev. B **102**, 214415 (2020).

[17] R. Schlitz, S. Vélez, A. Kamra, C. H. Lambert, M. Lammel, S. T. B. Goennenwein, and P. Gambardella, Control of nonlocal magnon spin transport via magnon drift currents, Phys. Rev. Lett. **126**, 257201 (2021).

[18] Janine Gückelhorn, Sebastián de-la-Peña, Monika Scheufele, Matthias Grammer, Matthias Opel, Stephan Geprägs, Juan Carlos Cuevas, Rudolf Gross, Hans Huebl, Akashdeep Kamra, and Matthias Althammer, Observation of the nonreciprocal magnon Hanle effect, Phys. Rev. Lett. **130**, 216703 (2023).

[19] J. Han, Y. Fan, B. C. McGoldrick, J. Finley, J. T. Hou, P. Zhang, and L. Liu, Nonreciprocal transmission of incoherent magnons with asymmetric diffusion length, Nano Lett. **21**, 7037 (2021).

[20] L. J. Cornelissen, J. Liu, B. J. van Wees, and R. A. Duine, Spin-current-controlled modulation of the magnon spin conductance in a three-terminal magnon transistor, Phys. Rev. Lett. **120**, 097702 (2018).

[21] T. Wimmer, M. Althammer, L. Liensberger, N. Vlietstra, S. Geprägs, M. Weiler, R. Gross, and H. Huebl, Spin transport in a magnetic insulator with zero effective dDamping, Phys. Rev. Lett. **123**, 257201 (2019).

[22] K. S. Das, F. Feringa, M. Middelkamp, B. J. van Wees, and I. J. Vera-Marun, Modulation of magnon spin transport in a magnetic gate transistor, Phys. Rev. B **101**, 054436 (2020).

[23] M. Collet, X. de Milly, O. d'Allivy Kelly, V. V. Naletov, R. Bernard, P. Bortolotti, J. Ben Youssef, V. E. Demidov, S. O. Demokritov, J. L. Prieto, M. Muñoz, V. Cros, A. Anane, G. de Loubens, and O. Klein, Generation of coherent spin-wave modes in yttrium iron garnet microdiscs by spin-orbit torque, Nat. Commun. **7**, 10377 (2016).

[24] J. Sinova, S. O. Valenzuela, J. Wunderlich, C. H. Back, and T. Jungwirth, Spin Hall effects, Rev. Mod. Phys. **87**, 1213 (2015).

[25] G. Sala, H. Wang, W. Legrand, and P. Gambardella, Orbital Hanle magnetoresistance in a 3d transition metal, Phys. Rev. Lett. **131**, 156703 (2023).

[26] T. Gao, A. Qaiumzadeh, H. An, A. Musha, Y. Kageyama, J. Shi, and K. Ando, Intrinsic spin-orbit torque arising from the Berry curvature in a metallic-magnet/Cu-oxide interface, Phys. Rev. Lett. **121**, 017202 (2018).

[27] G. Sala and P. Gambardella, Giant orbital Hall effect and orbital-to-spin conversion in 3d, 5d, and 4f metallic heterostructures, Phys. Rev. Res. **4**, 033037 (2022).

[28] H. Hayashi, D. Jo, D. Go, T. Gao, S. Haku, Y. Mokrousov, H. W. Lee, and K. Ando, Observation of long-range orbital transport and giant orbital torque, Commun. Phys. **6**, 32 (2023).

[29] D. Go, D. Jo, T. Gao, K. Ando, S. Blügel, H. W. Lee, and Y. Mokrousov, Orbital Rashba effect in a surface-oxidized Cu film, Phys. Rev. B **103**, L121113 (2021).

[30] D. Go, J. P. Hanke, P. M. Buhl, F. Freimuth, G. Bihlmayer, H. W. Lee, Y. Mokrousov, and S. Blügel, Toward surface orbitronics: Giant orbital magnetism from the orbital Rashba effect at the surface of sp-metals, Sci. Rep. **7**, 46742 (2017).

[31] D. Go, D. Jo, C. Kim, and H. W. Lee, Intrinsic spin and orbital Hall effects from orbital texture, Phys. Rev. Lett. **121**, 086602 (2018).

[32] H. An, Y. Kageyama, Y. Kanno, N. Enishi, and K. Ando, Spin-torque generator engineered by natural oxidation of Cu, Nat. Commun. **7**, 13069 (2016).

[33] L. Salemi, M. Berritta, A. K. Nandy, and P. M. Oppeneer, Orbitally dominated Rashba-Edelstein effect in noncentrosymmetric antiferromagnets, Nat. Commun. **10**, 5381 (2019).

[34] D. Go, D. Jo, H. W. Lee, M. Kläui, and Y. Mokrousov, Orbitronics: Orbital currents in solids, Europhys. Lett. **135**, 37001 (2021).

[35] Y. G. Choi, D. Jo, K. H. Ko, D. Go, K. H. Kim, H. G. Park, C. Kim, B. C. Min, G. M. Choi, and H. W. Lee, Observation of the orbital Hall effect in a light metal Ti, Nature (London) **619**, 52 (2023).

[36] I. Lyalin, S. Alikhah, M. Berritta, P. M. Oppeneer, and R. K. Kawakami, Magneto-optical detection of the orbital Hall effect in chromium, Phys. Rev. Lett. **131**, 156702 (2023).

[37] H. Hayashi and K. Ando, Orbital Hall magnetoresistance in Ni/Ti bilayers, Appl. Phys. Lett. **123**, 172401 (2023).

[38] S. Ding, Z. Liang, D. Go, C. Yun, M. Xue, Z. Liu, S. Becker, W. Yang, H. Du, C. Wang, Y. Yang, G. Jakob, M. Kläui, Y. Mokrousov, and J. Yang, Observation of the orbital Rashba-Edelstein magnetoresistance, Phys. Rev. Lett. **128**, 067201 (2022).

[39] S. Ding, A. Ross, D. Go, L. Baldrati, Z. Ren, F. Freimuth, S. Becker, F. Kammerbauer, J. Yang, G. Jakob, Y. Mokrousov, and M. Kläui, Harnessing orbital-to-spin conversion of interfacial orbital currents for efficient spin-orbit torques, Phys. Rev. Lett. **125**, 177201 (2020).

[40] J. Kim, D. Go, H. Tsai, D. Jo, K. Kondou, H. W. Lee, and Y. Otani, Nontrivial torque generation by orbital angular momentum injection in ferromagnetic-metal/Cu/Al_2O_3 trilayers, Phys. Rev. B **103**, L020407 (2021).

[41] J. Kim, J. Uzuhashi, M. Horio, T. Senoo, D. Go, D. Jo, T. Sumi, T. Wada, I. Matsuda, T. Ohkubo, S. Mitani, H.-W. Lee, and Y. Otani, Oxide layer dependent orbital torque efficiency in ferromagnet/Cu/oxide heterostructures, Phys. Rev. Mater. **7**, L111401 (2023).

[42] S. Lee, M.-G. Kang, D. Go, D. Kim, J.-H. Kang, T. Lee, G.-H. Lee, J. Kang, N. Jong Lee, Y. Mokrousov, S. Kim, K.-J. Kim, K.-J. Lee, and B.-G. Park, Efficient conversion of orbital Hall current to spin current for spin-orbit torque switching, Commun. Phys. **4**, 234 (2021).

[43] Q. K. Huang, S. Liu, T. Yang, R. Xie, L. Cai, Q. Cao, W. Lü, L. Bai, Y. Tian, and S. Yan, Current-induced magnetization switching in light-metal-oxide/ferromagnetic-metal bilayers via orbital Rashba effect, Nano Lett. **23**, 11323 (2023).

[44] A. Bose, F. Kammerbauer, R. Gupta, D. Go, Y. Mokrousov, G. Jakob, and M. Kläui, Detection of long-range orbital-Hall torques, Phys. Rev. B **107**, 134423 (2023).

[45] H. Hayashi, D. Go, Y. Mokrousov, and K. Ando, Observation of orbital pumping, arXiv:2304.05266.

[46] P. Wang, Z. Feng, Y. Yang, D. Zhang, Q. Liu, Z. Xu, Z. Jia, Y. Wu, G. Yu, X. Xu, and Y. Jiang, Inverse orbital Hall effect and orbitronic terahertz emission observed in the materials with weak spin-orbit coupling, npj Quantum Mater. **8**, 28 (2023).

[47] R. Xu, H. Zhang, Y. Jiang, H. Cheng, Y. Xie, Y. Yao, D. Xiong, Z. Zhu, X. Ning, R. Chen, Y. Huang, S. Xu, J. Cai, Y. Xu, T. Liu, and W. Zhao, Giant orbit-to-charge conversion induced via the inverse orbital Hall effect, arXiv: 2308.13144.

[48] A. El Hamdi, J. Y. Chauleau, M. Boselli, C. Thibault, C. Gorini, A. Smogunov, C. Barreteau, S. Gariglio, J. M. Triscone, and M. Viret, Observation of the orbital inverse Rashba–Edelstein effect, Nat. Phys. **19**, 1855 (2023).

[49] E. Santos, J. E. Abrão, D. Go, L. K. De Assis, Y. Mokrousov, J. B. S. Mendes, and A. Azevedo, Inverse orbital torque via spin-orbital intertwined states, Phys. Rev. Appl. **19**, 014069 (2023).

[50] E. Santos, J. E. Abrão, A. S. Vieira, J. B. S. Mendes, R. L. Rodríguez-Suárez, and A. Azevedo, Exploring orbital-charge conversion mediated by interfaces with copper through spin-orbital pumping, Phys. Rev. B **109**, 014420 (2024).

[51] H. Isshiki, P. Muduli, J. Kim, K. Kondou, and Y. Otani, Phenomenological model for the direct and inverse Edelstein effects, Phys. Rev. B **102**, 184411 (2020).

[52] S. Krishnia, B. Bony, E. Rongione, L. M. Vincente-Arche, S. Collin, A. Fert, J.-M. George, N. Reyren, V. Cros, and H. Jaffrès, Quantifying the large contribution from orbital Rashba–Edelstein effect to the effective damping-like torque on magnetization, APL Mater. **12**, 051105 (2024).

[53] T. Kimura, Y. Otani, T. Sato, S. Takahashi, and S. Maekawa, Room-temperature reversible spin Hall effect, Phys. Rev. Lett. **98**, 156601 (2007).

[54] A. Brataas, B. van Wees, O. Klein, G. de Loubens, and M. Viret, Spin iIsulatronics, Phys. Rep. **885**, 1 (2020).

[55] See Supplemental Material at http://link.aps.org/supplemental/10.1103/PhysRevLett.132.226704 for more details on the nanodevice fabrication, linearity of the nonlocal signals, and a discussion on the energy ranges of electrically and thermally generated magnons, which includes Refs. [1,3,13,14,49,52,56–58].

[56] P. Jiménez-Cavero, I. Lucas, D. Bugallo, C. López-Bueno, R. Ramos, P. Antonio Algarabel, M. Ricardo Ibarra, F. Rivadulla, and L. Morellón, Quantification of the interfacial and bulk contributions to the longitudinal spin Seebeck effect, Appl. Phys. Lett. **118**, 092404 (2021).

[57] T. Kikkawa, K. I. Uchida, S. Daimon, Z. Qiu, Y. Shiomi, and E. Saitoh, Critical suppression of spin Seebeck effect by magnetic fields, Phys. Rev. B **92**, 064413 (2015).

[58] K. An, R. Kohno, N. Thiery, D. Reitz, L. Vila, V. V. Naletov, N. Beaulieu, J. Ben Youssef, G. de Loubens, Y. Tserkovnyak, and O. Klein, Short-range thermal magnon diffusion in magnetic garnet, Phys. Rev. B **103**, 174432 (2021).

[59] F. K. Dejene, J. Flipse, and B. J. van Wees, Verification of the Thomson-Onsager reciprocity relation for spin caloritronics, Phys. Rev. B **90**, 180402(R) (2014).

[60] G. Okano, M. Matsuo, Y. Ohnuma, S. Maekawa, and Y. Nozaki, Nonreciprocal spin current generation in surface-oxidized copper films, Phys. Rev. Lett. **122**, 217701 (2019).

[61] S. A. Bender, R. A. Duine, and Y. Tserkovnyak, Electronic pumping of quasiequilibrium Bose-Einstein-condensed magnons, Phys. Rev. Lett. **108**, 246601 (2012).

[62] Y. Tokura and N. Nagaosa, Orbital physics in transition-metal oxides, Science **288**, 462 (2000).